Journal of Zhejiang University-SCIENCE C (Computers & Electronics)
ISSN 1869-1951 (Print); ISSN 1869-196X (Online)
www.zju.edu.cn/jzus; www.springerlink.com
E-mail: jzus@zju.edu.cn

Microfabrication technology for non-coplanar resonant beams and crab-leg supporting beams of dual-axis bulk micromachined resonant accelerometers*

Jian-qiang HAN†, Ri-sheng FENG, Yan LI, Sen-lin LI, Qing LI

(*College of Mechanical & Electrical Engineering, China Jiliang University, Hangzhou 310018, China*)

†E-mail: hjqsmx@sina.com

Received Aug. 24, 2012; Revision accepted Nov. 19, 2012; Crosschecked Dec. 14, 2012

Abstract: This paper presents the design principles and fabrication techniques for simultaneously forming non-coplanar resonant beams and crab-leg supporting beams of dual-axis bulk micromachined resonant accelerometers by masked-maskless combined anisotropic etching. Four resonant beams are located at the surface of a silicon substrate, whereas the gravity centre of a proof mass lies within the neutral plane of four crab-leg supporting beams on the same substrate. Compared with early reported mechanical structures, the simple structure not only eliminates the bending moments caused by in-plane acceleration, and thereby avoiding the rotation of the proof mass, but also providing sufficiently small rigidity to *X* and *Y* axes accelerations, potentially leading to a large sensitivity for measuring the in-plane acceleration.

Key words: Resonant accelerometer, Maskless etching, Bulk micromachining technology, Microelectromechanical system (MEMS), Microsensor

doi:10.1631/jzus.C1200251 **Document code:** A **CLC number:** TP212

1 Introduction

With the help of microelectromechanical system (MEMS) technology, various types of miniaturized accelerometers have been developed. Among these accelerometers, resonant accelerometers were reported to have good properties such as large dynamic range and high sensitivity. In addition, the quasi-digital nature of the output frequency signal eases interfacing to readout and signal conditioning circuit. Generally, a resonant accelerometer consists of a proof mass supported by one or several elastic supporting beams and resonators. The resonant frequency of resonators changes with the applied acceleration. As a result, the applied acceleration can be detected by the changes in resonant frequency.

Resonant accelerometers can be fabricated by means of bulk micromachining (Burns *et al*., 1996; Burrer *et al.*, 1996; Ferrari *et al*., 2005; Chen *et al*., 2009; Qiu *et al*., 2009; Wang *et al*., 2011), surface micromaching (Roessig *et al*., 1997; Seok *et al*., 2002; Seshia *et al*., 2002; Comi *et al*., 2009; 2010; 2011; Olsson *et al*., 2009), bulk and surface mixed micromachining (Seok *et al.*, 2002; Seok and Chun, 2006), and silicon on insulator (SOI) technology (Su *et al.*, 2005; Pinto *et al.*, 2009). Compared to other resonant accelerometers, resonant accelerometers fabricated by means of bulk micromachining technology have the advantage of high sensitivity because full-wafer thick silicon proof mass can be achieved.

Among a variety of resonators based on different excitation and detection principles, electrothermal excitation/piezoresistive detection and electrostatic excitation/capacitive detection resonators are more attractive from a technological point of view. In fabricating resonant accelerometers based on these two excitation and detection principles, thin resonant beams should be situated at the top surface of

* Project (No. 61076110) supported by the National Natural Science Foundation of China

substrates to easily pattern the configuration of resistors for electrothermal excitation/piezoresistive detection or electrode plates for electrostatic excitation/capacitive detection. The gravity centre of the proof mass must lie within the neutral plane of supporting beams to avoid rotation of the proof mass under in-plane acceleration (Huang *et al*., 2003). Therefore, fabrication of non-coplanar resonant beams and supporting beams is a key technique for developing bulk micromachined resonant accelerometers. Different methods have been used to realize this goal in the past. Burrer *et al*. (1996) presented a resonant accelerometer made from two bonded wafers. A resonant beam is situated at the top surface of the upper wafer. Four 20-μm-thick hinges, angled with respect to the <110> crystal orientation and located at the top surface of the lower wafer, support the proof mass. The geometries of the two proof mass parts are dimensioned such that their center of gravity lies within the neutral plane of the supporting hinges. Consequently, bending moments caused by in-plane accelerations are practically eliminated. The complex mechanical structure of the resonant accelerometer requires at least four layers bonding to realize subsequent vacuum packaging. Burns *et al*. (1996) fabricated a resonant accelerometer consisting of a highly symmetric proof mass and flexures at both sides of the chip. The proof mass is suspended by a series of flexures and struts. The flexures are located at the center of each side and the struts are located at the corners. The fabrication process requires double-sided epitaxy process on both sides of polished silicon substrates. In addition, large residual stress in flexures and struts inevitably influences the long-term stability of sensors.

It is well known that resonant accelerometers have the advantage of high sensitivity, but the sensitivity of most reported resonant accelerometers ranges only from several Hz/g to several hundred Hz/g, as summarized in Table 1, except for a few accelerometers sensing *Z* axis acceleration (Chen *et al*., 2009; Wang *et al*., 2011). Therefore, improving the in-plane acceleration sensitivity is another key task for designing and fabricating a resonant accelerometer. Supporting a proof mass with clamped-clamped beams is a feasible mechanical structure of dual-axis resonant accelerometer for sensing the in-plane acceleration. However, larger Young's modulus of silicon materials diminishes the in-plane acceleration sensitivity. Double-ended tuning fork (DETF) is

Table 1 Sensitvity of reported resonant accelerometers

Fabrication process	Axis	Resonator	Supporting beam	Static sensitivity (Hz/g)	Resonance frequency (kHz)	Reference
Bulk micromachining	*Z*	Bridge	Cantilever	260 180	71.7 91.8	Burrer *et al.*, 1996
	Z	Bridge	Symmetrical beam	700	733.2	Burns *et al.*, 1996
	Z	Bridge	Cantilever	35	70	Ferrari *et al.*, 2005
	X	DETF	Microleverage	14.35	88.64	Qiu *et al.*, 2009
	Z	Triple beam	Cantilever	1500	67.15	Chen *et al.*, 2009
	Z	Bridge	Microleverage	1900	67.885	Wang *et al.*, 2011
Surface micromaching	*X*	DETF	Microleverage	2.4 45	175 68	Roessig *et al.*, 1997
	X	DETF	Microleverage	17	173	Seshia *et al.*, 2002
	X, *Y*	Bridge	Beam	201	84	Seok *et al.*, 2002
	X	DETF	Folded-beam	3.4	890	Olsson *et al.*, 2009
	X	Bridge	Thin beam	450	50	Comi *et al.*, 2009
	X, *Y*	Torsion beam		128	23.4	Comi *et al.*, 2010
	Z			73	12.716	Comi *et al.*, 2011
Mixed micromachining	*Z*	Torsion beam		8.125	6.928	Seok *et al.*, 2002
	X	DETF	Beam	128	23.4	Seok and Chun, 2006
Silicon on insulator (SOI) technology	*X*	DETF	Two-stage microleverage	158	131	Su *et al.*, 2005
	Z	Bridge	Beam	22	459.152	Pinto *et al.*, 2009

DETF: double-ended tuning fork

preferred as opposed to the clamped-clamped beam. However, DETF is somewhat complicated, flimsy, and difficult to fabricate by bulk micromaching technology. Replacing hardy clamped-clamped beams with crab-leg supporting beams is a feasible approach to improve sensitivity for detecting the in-plane acceleration. This kind of supporting beam has been used in surface micromaching capacitive accelerometers by Manut and Syono (2006) for sensing out-of-plane acceleration. Fedder (1994) analyzed the spring constant of crab-leg supporting beams with a rectangular cross section in *X*, *Y*, and *Z* directions. In this paper, we primarily commit ourselves to researching the microfabrication technology and design principles for simultaneously forming non-coplanar resonant beams and crab-leg supporting beams of dual-axis bulk micromachined resonant accelerometers.

2 Mechanical structures of resonant accelerometers

The mechanical structure of dual-axis bulk micromachined resonant accelerometers to be fabricated is shown in Fig. 1. A proof mass is supported by four elastic crab-leg supporting beams and four thin resonant beams. One end of the resonant beams or crab-leg supporting beams is fixed on the frame, and the other end on the proof mass. Thin resonant beams are located at the top surface of the chip, whereas the gravity centre of the proof mass lies within the neutral plane of four crab-leg supporting beams on the same chip to avoid the rotation of the proof mass under in-plane acceleration. The thickness of the proof mass, resonant beams, and crab-leg supporting beams are *H*, *h*, and *d*, respectively. The width of groove and the side length of the proof mass are *L* and L_m, respectively. The diamond-shaped crab-leg supporting beams are enveloped by {113} planes (Fig. 2l). The included angles of side face are 50.48° and 129.52°, respectively. As a result, the width of supporting beams is equal to 2.12*d*.

The flexure spring constant of a single crab-leg supporting beam with a diamond-shaped cross section in the *X*-direction can be calculated according to the analysis method suggested by Fedder (1994) for beams with rectangular cross sections as

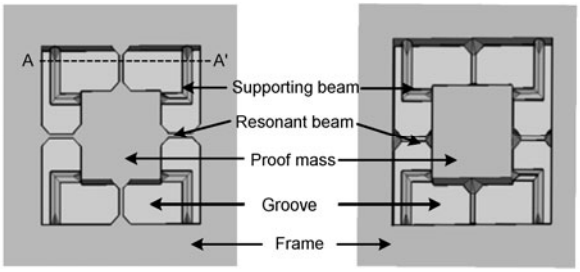

Fig. 1 Mechanical structures of dual-axis resonant accelerometers viewed from both front (left) and back (right) sides of the chip

$$K_X = \frac{Edw_b^3(4L_b + \alpha L_a)}{32L_b^3(L_b + \alpha L_a)}, \tag{1}$$

where the coefficient α is as

$$\alpha = \frac{I_b}{I_a} = \left(\frac{w_b}{w_a}\right)^3, \tag{2}$$

E is Young's modulus of silicon materials, L_a and w_a are the length and width of the thigh segment, respectively, and L_b and w_b are the length and width of the shin segment, respectively. For the designed crab-leg supporting beams, the thigh segment has the same width as the shin segment, as a result, α=1. Assuming L_a=0.5L_b, the flexure spring constant of the crab-leg supporting beams in the *X*-direction can be calculated as

$$K_X = 0.893\frac{Ed^4}{L_b^3}. \tag{3}$$

Supporting the proof mass with clamped-clamped beams is a feasible mechanical structure of the dual-axis resonant accelerometer for sensing in-plane acceleration. Supposing that the clamped-clamped supporting beam has the same diamond-shaped cross section as that of the crab-leg supporting beam, the longitudinal deformation of a clamped-clamped beam is proportional to the longitudinal stress in the elastic range. The proportionality constant of the longitudinal stress and strain is the elastic modulus E of the material,

$$E = \frac{F/A}{\Delta L_s / L_s} = \frac{L_s}{A}\frac{F}{\Delta L_s}, \tag{4}$$

where F is the longitudinal stress, A and L_s are the cross-sectional area and length of the clamped-clamped beam, respectively. So the flexure spring constant of a clamped-clamped supporting in the X-direction can be calculated as

$$k_X = \frac{F}{\Delta L_s} = \frac{EA}{L_s} = 1.06\frac{Ed^2}{L_s}. \quad (5)$$

Supposing the length of the clamped-clamped beam L_s is equal to that of shin segment L_b, the ratio of the spring constant of a crab-leg supporting beam to that of a clamped-clamped supporting beam with the same diamond-shaped cross section is

$$\frac{K_X}{k_X} = 0.842\left(\frac{d}{L_b}\right)^2. \quad (6)$$

Since the thickness d of a crab-leg supporting beam is far less than the length of the shin segment L_b, Eq. (6) indicates that the crab-leg supporting beam is more flexible than the clamped-clamped supporting beam under in-plane acceleration.

3 Fabrication techniques

The mechanical structures of dual-axis bulk micromachined resonant accelerometers are fabricated by five photolithographic steps, two masked wet anisotropic etching steps, and one masked-maskless combined anisotropic etching step. As shown in Fig. 2a, a thick silicon oxide film is first thermally grown on both sides of (100) oriented silicon wafers. Subsequently, the SiO_2 film at the backside of the wafer is patterned for undercutting four resonant beams (Fig. 2b). The width and length of four openings are b+2(H−h)cot54.7° and L, respectively, where b is the mask width of resonant beams at the front side of wafers in the following photolithography. Subsequently, the SiO_2 film in four openings is removed by buffered HF solution. The first masked anisotropic wet etching is performed from the backside of the wafers and forms four pyramidal pits with the depth of H_1 (Fig. 2c).

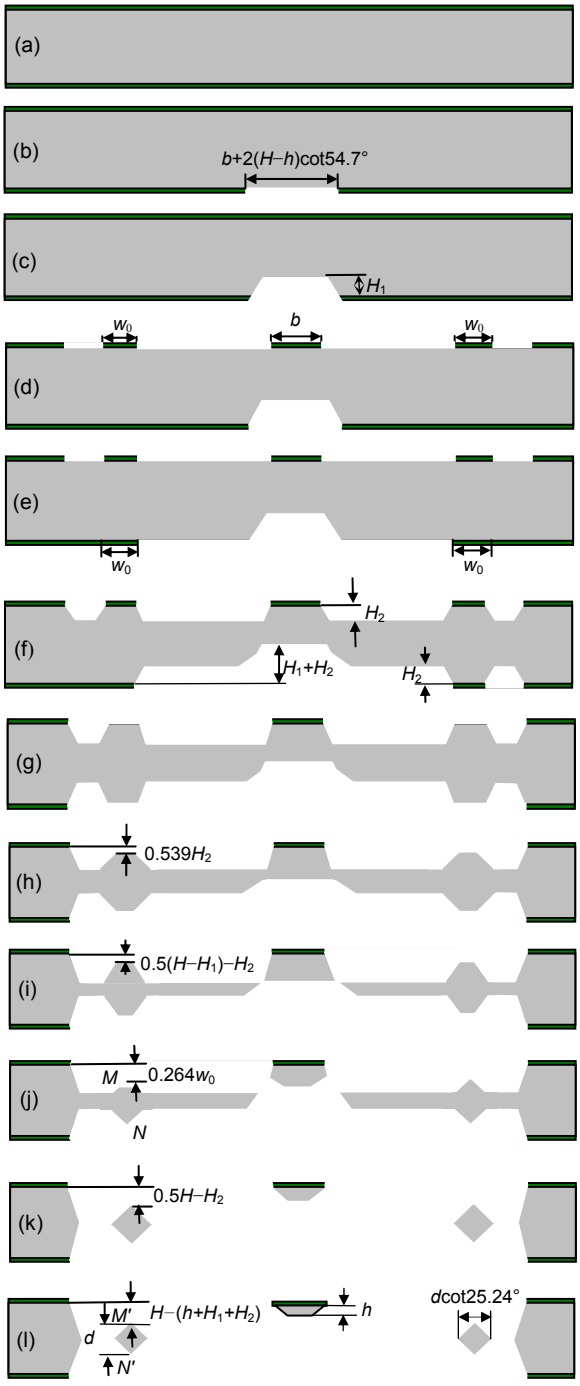

Fig. 2 Fabrication sequence for simultaneous formation of resonant beams and crab-leg supporting beams by masked-maskless combined anisotropic etching along the direction of A-A′ denoted in Fig. 1

(a) Oxidation; (b)–(c) Etching from the backside of the wafers; (d)–(f) Photolithography and etching groove from both sides of wafers; (g) Removing the mask of crab-leg supporting beams; (h)–(l) Masked-maskless combined anisotropic etching

The next step is to pattern the groove at both sides of wafers shown in Figs. 2d and 2e. The mask for patterning the groove is shown in Fig. 3. The mask widths of supporting beams and resonant beams are w_0 and b, respectively. The SiO_2 film in the dark area is removed by buffered HF solution. Subsequently, the silicon wafers are etched in KOH solution again (Fig. 2f). The silicon in both sides of the groove is removed to a depth of H_2 ($H_2>d/2$). Four pyramidal pits etched in the first masked wet etching are further undercut to a depth of H_1+H_2. Subsequently, the mask of crab-leg supporting beams on both sides of the wafer is patterned and removed by buffered HF solution (Fig. 2g).

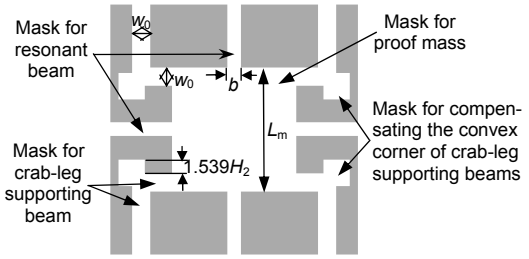

Fig. 3 Mask for patterning the groove on both sides of wafers

The last step is masked-maskless combined anisotropic etching in 40% KOH solution for simultaneous formation of resonant beams and crab-leg supporting beams. The continuing geometric evolution of the mechanical structure during the etching process is discussed in the following sections.

1. The (111) sidewall of crab-leg supporting beams disappears at the etching depth of $0.539H_2$

The (111) oriented sidewall of crab-leg supporting beams etched in the second masked wet etching is cut by (113) fast-etching planes during the masked-maskless combined anisotropic etching. The included angle between the (113) plane and the (100) plane is θ with $\tan\theta=\sqrt{2}/3$ (or θ=25.24°) (Li *et al.*, 1996). The (111) sidewalls are completely replaced by (113) fast-etching planes (Fig. 2h), when the vertical etching depth of the (100) plane reaches

$$H_3(t_1) = H_2/(1.658r_3 - 1), \tag{7}$$

where r_3 is the ratio of the etching rates of (113) fast-etching planes and (100) planes. r_3 decreases with the increase of the concentration of KOH solution. For 40% KOH solution, r_3=1.71. As a result, (111) oriented sidewall of crab-leg supporting beams etched in 40% KOH solution is replaced completely by (113) fast-etching planes when the vertical etching depth reaches $0.539H_2$.

2. The resonant beams are released at the etching depth of $0.5(H-H_1)-H_2$

As shown in Fig. 2i, the resonant beams are released when the vertical etching depth in the masked-maskless combined anisotropic etching reaches

$$H_3(t_2) = 0.5(H - H_1) - H_2. \tag{8}$$

The thickness of resonant beams at the etching depth can be calculated as $0.5(H-H_1)$. However, these resonant beams are still thicker than the designed.

3. The top and bottom surfaces of supporting beams disappear at the etching depth of $0.264w_0$

The width of top and bottom surfaces of crab-leg supporting beams etched in 40% KOH solution reduces with the lateral recession of the intersection of (113) plane according to Eq. (9) (Li *et al.*, 1996):

$$\begin{aligned} w &= w_0 - 2(2.3452r_3 - 2.1213)H_3(t) \\ &= w_0 - 3.78H_3(t). \end{aligned} \tag{9}$$

As a result, the top and bottom surfaces of crab-leg supporting beams disappear (Fig. 2j), when the vertical etching depth reaches

$$H_3(t_3) = 0.264w_0. \tag{10}$$

4. The crab-leg supporting beams are released at the etching depth of $0.5H-H_2$

The groove is penetrated by KOH solution from both sides of wafers during the second masked wet etching and the masked-maskless combined anisotropic etching. The crab-leg supporting beams are released (Fig. 2k), when the etching depth reaches

$$H_3(t_4) = 0.5H - H_2. \tag{11}$$

5. The resonant beams reach the designed thickness at the etching depth of $H-(h+H_1+H_2)$

The undercutting depths of resonant beams in the first masked etching and the second masked

etching are H_1 and H_2, respectively. To thin the resonant beams to the designed thickness h, the final etching depth $H_3(t_5)$ during the masked-maskless combined etching step must be

$$H_3(t_5) = H - (h + H_1 + H_2). \tag{12}$$

6. The vertical etching depth at which supporting beams reach the designed thickness depends on the mask width of supporting beams

Apparently, if the mask of supporting beams is wider than $3.78(H_3(t_5))$, the supporting beams reach the designed thickness at the final etching depth:

$$H_3(t_5) = 0.5(H - d). \tag{13}$$

If the mask of supporting beams is narrower than $3.78(H_3(t_5))$, the top and bottom surfaces of crab-leg supporting beams disappear before the supporting beams reach the designed thickness. Under the circumstances, the recess of the (113) fast-etching planes removes the top and bottom edges of crab-leg supporting beams from M, N to M', N', respectively with the proceed of maskless etching, as shown in Figs. 2j, 2k, 2l, and 4. The cross section of finally etched crab-leg supporting beams is $P'M'Q'N'$ with $M'N'=d$. The recessional distance (LM') of the (113) fast-etching planes is 1.72 times as large as the vertical etching depth (H') of the (100) plane (Li *et al*., 1996). As a result, the recessional distance of top edge is

$$MM' = LM' / \cos 25.24° = 1.89H', \tag{14}$$

where H' is the vertical etching depth of the (100) plane in the period from time t_3 to t_5. The thickness of crab-leg supporting beams can be calculated as

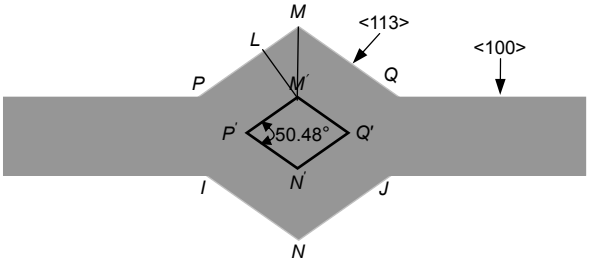

Fig. 4 Geometric evolution of the cross section of crab-leg supporting beams in the period from time t_3 to t_5

$$d = H - 2(0.264w_0 + 1.89H'). \tag{15}$$

H' can be calculated from Eq. (15) as

$$H' = 0.264(H - d - 0.528w_0). \tag{16}$$

The final vertical etching depth of the (100) plane during the masked-maskless combined anisotropic etching can be calculated from Eq. (16) as

$$H_3(t_5) = 0.264w_0 + H' = 0.264(H - d + 0.472w_0). \tag{17}$$

In addition, the total vertical etching depth of the second masked wet etching and the masked-maskless combined etching must be lager than half the original thickness of the wafers to release the crab-leg supporting beams, that is

$$H_2 + H_3(t_5) \geq H/2. \tag{18}$$

In essence, the etching depth during the first masked etching (H_1), the second masked etching (H_2), and the final masked-maskless combined anisotropic etching ($H_3(t_5)$) must satisfy Eqs. (12), (13), and (18) simultaneously if the mask for supporting beams is wider than $3.78H_3(t_5)$; otherwise, these parameters should satisfy Eqs. (12), (17), and (18) simultaneously.

4 Principles of structure design

4.1 Geometry of the resonant beams

As mentioned above, the thickness of resonant beams is $0.5(H-H_1)$ when they are released at the masked-maskless combined anisotropic etching depth of $0.5(H-H_1)-H_2$. Since the included angle between the (111) sidewall and the (100) top plane of resonant beams is 54.7°, the width of the bottom surface of resonant beams at the etching depth can be calculated as $b+(H-H_1)\cot 54.7°$.

The vertical etching depth from $H_3(t_2)$ to $H_3(t_5)$ is equal to

$$\begin{aligned} &H_3(t_5) - H_3(t_2) \\ &= [H - (h + H_1 + H_2)] - [0.5(H - H_1) - H_2] \\ &= 0.5(H - H_1) - h. \end{aligned} \tag{19}$$

As a result, the final width of the bottom plane can be calculated as

$$b' = b + (H - H_1)\cot 54.7° - 3.78[0.5(H - H_1) - h]$$
$$= b + 1.182(H_1 - H) + 3.78h. \quad (20)$$

If $b'>0$, the cross section of resonant beams is an isosceles trapezoid. The width of the top plane is $b'+2h\cot 25.24°$. On the contrary, the cross section of resonant beams is an isosceles triangle. The width of the top plane is $2h\cot 25.24°$.

While the width of resonant beams is shaped by maskless wet etching, the clamped ends of resonant beams fixed between the frame and the proof mass are etched by masked wet etching. The effective length of resonant beams can be calculated as

$$L_r = L - 2(H - h)\cot 54.7°. \quad (21)$$

4.2 Mask for compensating the convex corners of crab-leg supporting beams

To preserve the shape of the convex corners during anisotropic etching, various corner compensation structures such as square (Puers and Sansen, 1990), triangular (Wu and Ko, 1989), <100> bars (Mayer *et al*., 1990; Zhang *et al*., 1996), and <110> strip patterns (Bao *et al*., 1993) have been used in the past. In this paper, square patterns are used to preserve the convex corners of crab-leg supporting beams because it occupies minimum dimension.

If convex corner compensation is used in masked wet anisotropic etching and a good compensation effect is obtained, the top of the convex corner will remain straight during the subsequent maskless etching process. However, the bottom of the convex corner is seriously undercut in the subsequent maskless etching. To maintain the convex corner in good shape during the maskless etching process, it must be ensured that the compensation pattern is not completely depleted when the maskless etching depth reaches $0.539H_2$ (Li *et al*., 1996). Therefore, the side length of the square compensation pattern should be equal to $2(H_2+0.539H_2)$.

4.3 Side length of the square proof mass

As shown in Fig. 3, the side length of the square proof mass must be larger than the sum of the width of openings for undercutting resonators, side length of the square patterns for compensating convex corner and the twice width of mask for crab-leg supporting, that is

$$L_m > b + 2(H - h)\cot 54.7° + 2w_0 + 2(H_2 + 0.539H_2). \quad (22)$$

5 Experiment and results

5.1 Illustrating the designing principles and fabricating techniques

The optimization design of the mechanical structure relates to the measuring range and the excitation/detection method. In this section, we justify only the validity of the presented design principles. The thickness of silicon wafers is 371 μm. The designed thickness of resonant beams and supporting beams are 10 and 50 μm, respectively. The effective length of resonant beams to be fabricated is 600 μm. As a result, the width of the groove (L) is calculated as 1111.2 μm from Eq. (21).

The etching depth during the first masked etching (H_1), the second masked etching (H_2), and the masked-maskless combined anisotropic etching ($H_3(t_5)$) should satisfy Eqs. (12), (17), and (18) simultaneously. In addition, the etching depth of masked-maskless combined anisotropic etching ($H_3(t_5)$) should be large enough in order that the wafers have enough strength to endure the last photolithography process. On the other hand, large $H_3(t_5)$ reduces the mask dimension for compensating the convex corner of crab-leg supporting beams. The dimensions of the chips are also reduced because the second masked etching (H_2) decreases with increase in the masked-maskless combined anisotropic etching depth ($H_3(t_5)$) according to Eq. (18). Based on the above principles, the etching depths H_1, H_2, and $H_3(t_5)$ are allocated as 171, 50, and 140 μm, respectively.

The average width of designed resonant beams is 142 μm. Since the included angle between the (113) sidewall and the top plane of finally etched resonant beams is 25.24°, the widths of the bottom plane (b') and top plane (b'') are 163 and 121 μm, respectively. The mask width (b) of resonant beams can be calculated from Eq. (20) as 319.6 μm.

The mask width w_0 of supporting beams can be calculated from Eq. (17) as 444.8 μm. The width ($d$cot25.24°) of supporting beams with diamond-shaped cross sections (Fig. 2) should be equal to 106 μm.

5.2 Fabrication process

The fabrication process starts with n-type silicon wafers of resistivity between 3–6 Ω·cm. The main process flow is as follows:

1. A 1.5-μm silicon dioxide film is grown on both sides of wafers as etching mask at first (Fig. 2a).

2. Four openings are patterned on the backside of the wafer for undercutting resonant beams. The width and length of openings are 788.6 and 1111 μm, respectively (Fig. 2b).

3. Silicon wafers are etched in KOH solution (40%, 60 °C) for 8.64 h. The etching depth (H_1) is measured to be 171 μm with a Dektak 150 surface profiler (Fig. 2c).

4. The SiO_2 film in groove at both sides of the wafers is patterned and removed by buffered HF solution (Figs. 2d and 2e).

5. Silicon wafers are etched in 40% KOH solution at 60 °C again. The vertical etching depth (H_2) is 50 μm (Fig. 2f).

6. The mask for crab-leg supporting beams at both sides of wafers is patterned and removed by buffered HF solution (Fig. 2g).

7. The last step is masked-maskless combined anisotropic etching in 40% KOH solution at 60 °C for simultaneous formation of the resonant beams and crab-leg supporting beams. The vertical etching depth is 140 μm (Figs. 2h–2l).

5.3 Experimental results

The etched mechanical structures at etching depths of $H_3(0)$, $H_3(t_1=26.95\ \mu m)$, $H_3(t_2=50\ \mu m)$, $H_3(t_3=117.4\ \mu m)$, $H_3(t_4=135.5\ \mu m)$, and $H_3(t_5=140\ \mu m)$ are shown in Fig. 5. Figs. 5a, 5c, 5e, 5g, 5i, and 5k are the pictures taken from the front side of chips while Figs. 5b, 5d, 5f, 5h, 5j, and 5l are those taken from the back side. The finally etched resonant beams and crab-leg supporting beams at the masked-maskless combined anisotropic etching depth of 140 μm are shown in Figs. 5k and 5l. The average widths of supporting beams and resonant beams are measured with a 3D super-depth digital microscope (KEYENCE VHX-500FE) to be 210 and 138.1 μm, respectively. The deviation of width with theoretical value arises from several factors. Firstly, the widths of fabricated supporting beams and resonant beams are greatly dependent on the original wafer thickness. The deviation of 1 μm in thickness results in a 3.78 μm deviation in width of resonant beams and 7.8 μm deviation in width of supporting beams. Another factor is the difference in manufacturer and marque of KOH reagent with that used in Li *et al*. (1996). The reagent influences the ratio of the etching rates of (113) fast-etching planes and (100) planes.

The effective length of fabricated resonant beams is measured to be 720 μm. The deviations from the theoretical value are 9.75%. The fast etching of silicon around the clamped ends of the resonant beams increases the length of resonant beams.

As shown in Figs. 5k and 5l, we observe that the convex corners of crab-leg supporting beams are preserved perfectly. As for the eight convex corners of the proof mass, there is no preservation method because the SiO_2 film around the convex corners has been removed by buffered HF solution. Since the construction is symmetrical about the middle plane of the substrate, the undercutting of the convex corners has less adverse influence on the sensor performances.

6 Conclusions

This paper presents a method for simultaneously forming non-coplanar resonant beams and crab-leg supporting beams of dual-axis bulk micromachined resonant accelerometers on the same wafer by masked-maskless combined anisotropic etching. The cross section of crab-leg supporting beams is diamond-shaped. The included angles of the side face are 50.48° and 129.52°, respectively. The cross section of resonant beams is either an isosceles trapezoid or a triangle. Compared with early reported structures, the novel mechanical structures fabricated with masked-maskless combined anisotropic etching have advantages of high in-plane sensitivity and eliminate the bending moments caused by in-plane acceleration, and as a result, avoid the rotation of the proof mass.

It should be noticed that the thicknesses of the fabricated resonant beams and crab-leg supporting beams are directly dependent on the original

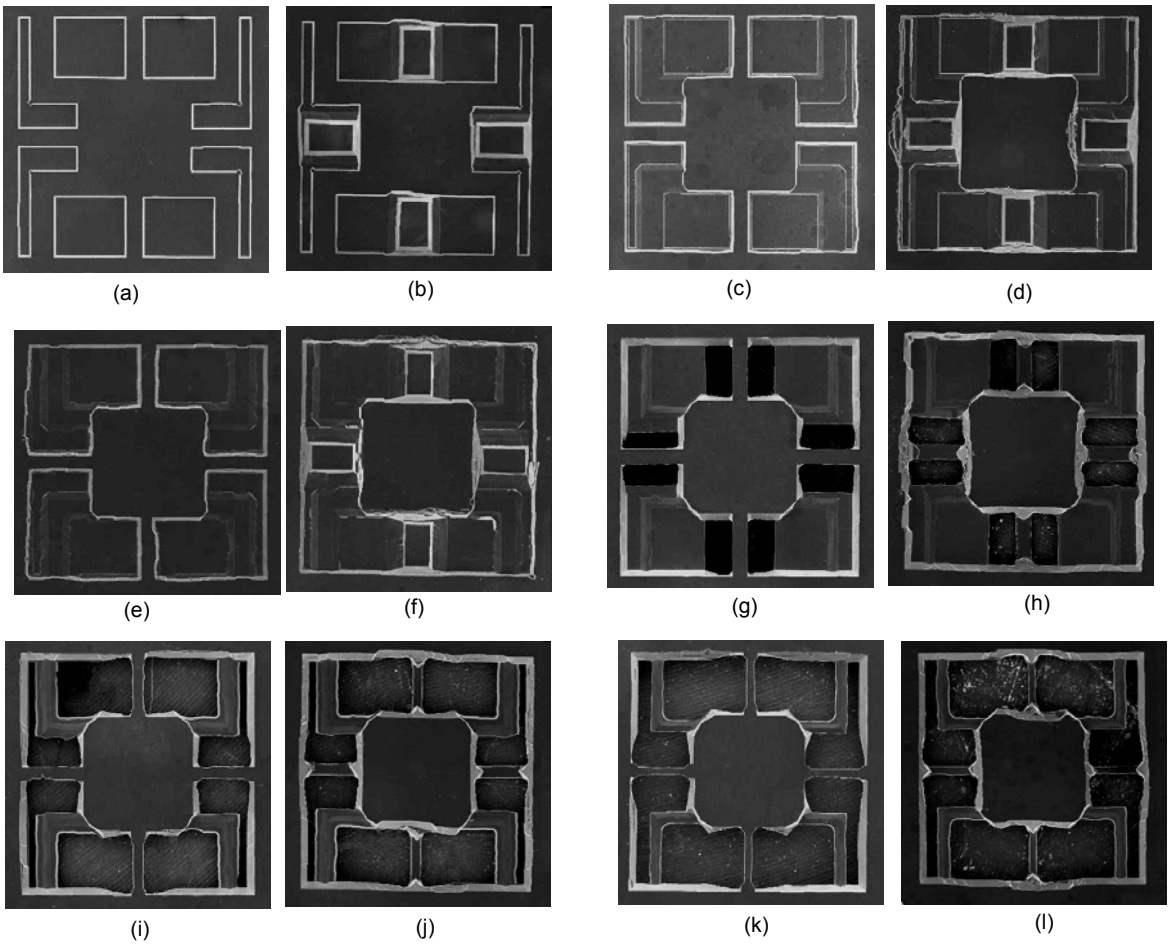

Fig. 5 Fabricated mechanical structures of dual-axis bulk micromachined resonant accelerometers at the depth of 0 μm (a and b), 26.95 μm (c and d), 50 μm (e and f), 117.4 μm (g and h), 135.5 μm (i and j), and 140 μm (k and l)
Figs. 5a, 5c, 5e, 5g, 5i, and 5k are taken from the front side of chips; Figs. 5b, 5d, 5f, 5h, 5j, and 5l are taken from the back side of chips

thickness of wafers and the thickness uniformity of the whole wafer. To accurately realize the mechanical structures of resonant accelerometers, the original thickness of wafers must be measured accurately and the thickness uniformity of the whole wafer must be controlled to a moderate tolerance range. In addition, the concentration of wet solution should keep constant in etching.

References

Bao, M., Burrer, C., Esteve, J., Bausells, J., Marco, S., 1993. Etching front control of <110> strips for corner compensation. *Sens. Actuat. A*, **37-38**:727-732. [doi:10.1016/0924-4247(93)80123-X]

Burns, D.W., Horning, R.D., Herb, W.R., Zook, J.D., Guckel, H., 1996. Sealed-cavity resonant microbeam accelerometer. *Sens. Actuat. A*, **53**(1-3):249-255. [doi:10.1016/0924-4247(96)01135-1]

Burrer, C., Esteve, J., Lora-Tamayo, E., 1996. Resonant silicon accelerometers in bulk micromachining technology—an approach. *J. Microelectromech. Syst.*, **5**(2):122-130. [doi:10.1109/84.506200]

Chen, D., Wu, Z., Liu, L., Shi, X., Wang, J., 2009. An electromagnetically excited silicon nitride beam resonant accelerometer. *Sensors*, **9**(3):1330-1338. [doi:10.3390/s90301330]

Comi, C., Corigliano, A., Langfelder, G., Longoni, A., Tocchio, A., Simoni, B., 2009. A New Two-Beam Differential Resonant Micro Accelerometer. IEEE Conf. on Sensors, p.158-163. [doi:10.1109/ICSENS.2009.5398209]

Comi, C., Corigliano, A., Langfelder, G., Longoni, A., Tocchio, A., Simoni, B., 2010. A High Sensitivity Uniaxial Resonant Accelerometer. IEEE 23rd Int. Conf. on Micro Electro Mechanical Systems, p.260-263. [doi:10.1109/MEMSYS.2010.5442517]

Comi, C., Corigliano, A., Langfelder, G., Longoni, A., Tocchio, A., Simoni, B., 2011. A New Biaxial Silicon Resonant Micro Accelerometer. IEEE 24th Int. Conf. on

Micro Electro Mechanical Systems, p.529-533. [doi:10.1109/MEMSYS.2011.5734478]

Fedder, G.K., 1994. Simulation of Microelectromechanical Systems. PhD Thesis, University of California, Berkeley.

Ferrari, V., Ghisla, A., Marioli, D., Taroni, A., 2005. Silicon resonant accelerometer with electronic compensation of input-output cross-talk. *Sens. Actuat. A*, **123-124**:258-266. [doi:10.1016/j.sna.2005.03.067]

Huang, P.S., Ren, T.L., Lou, Q.W., Liu, J.S., Liu, L.T., Li, Z.J., 2003. Design of a triaxial piezoelectric accelerometer. *Integr. Ferroelectr.*, **56**(1):1115-1122. [doi:10.1080/10584580390259722]

Li, X.X., Bao, M.H., Shen, S.Q., 1996. Maskless etching of three-dimensional silicon structures in KOH. *Sens. Actuat. A*, **57**(1):47-52. [doi:10.1016/S0924-4247(97)80094-5]

Manut, A., Syono, M.I., 2006. Effects of Mechanical Geometries on Resonance Sensitivity of MEMS Out-of-Plane Accelerometer. IEEE Int. Conf. on Semiconductor Electronics, p.25-28. [doi:10.1109/SMELEC.2006.381013]

Mayer, G.K., Offereings, H.L., Sandmaier, H., Kühl, K., 1990. Fabrication of non-underetched convex corner in anisotropic etching of (100) silicon in aqueous KOH with respect to novel micromechanical elements. *J. Electroch. Soc.*, **137**(12):3947-3951. [doi:10.1149/1.2086334]

Olsson, R.H., Wojciechowski, K.E., Baker, M.S., Tuck, M.R., Fleming, J.G., 2009. Post-CMOS-compatible aluminum nitride resonant MEMS accelerometers. *J. Microelectromech. Syst.*, **18**(3):671-678. [doi:10.1109/JMEMS.2009.2020374]

Pinto, D., Mercier, D., Kharrat, C., Colinet, E., Nguyen, V., Reig, B., Hentz, S., 2009. A Small and High Sensitivity Resonant Accelerometer. Proc. Eurosensors 23rd Conf. on Procedia Chemistry, p.536-539. [doi:10.1016/j.proche.2009.07.134]

Puers, B., Sansen, W., 1990. Compensation structures for convex corner micromachining in silicon. *Sens. Actuat. A*, **23**(1-3):1036-1041. [doi:10.1016/0924-4247(90)87085-W]

Qiu, A., Su, Y., Zhu, X., Shi, Q., 2009. Bulk-Micromachined Silicon Resonant Accelerometer. IEEE Int. Conf. on Information and Automation, p.1289-1292. [doi:10.1109/ICINFA.2009.5205115]

Roessig, T.A., Howe, R.T., Pisano, A.P., Smith, J.H., 1997. Surface-Micromachined Resonant Accelerometer. Proc. of Int. Solid State Sensors and Actuators Conf., p.859-862. [doi:10.1109/SENSOR.1997.635237]

Seok, S., Chun, K., 2006. Inertial-grade in-plane resonant silicon accelerometer. *Electr. Lett.*, **42**(19):1092-1094. [doi:10.1049/el:20061774]

Seok, S., Seong, S., Lee, B., Kim, J., Chun, K., 2002. A High Performance Mixed Micromachined Differential Resonant Accelerometer. Proc. IEEE Sensors, p.1058-1063. [doi:10.1109/ICSENS.2002.1037259]

Seshia, A.A., Palaniapan, M., Roessig, T.A., Howe, R.T., Gooch, R.W., Schimert, T.R., Montague, S., 2002. A vacuum packaged surface. *J. Microelectromech. Syst.*, **11**(6):784-793. [doi:10.1109/JMEMS.2002.805207]

Su, S.X.P., Yang, H.S., Agogino, A.M., 2005. A resonant accelerometer with two-stage microleverage mechanisms fabricated by SOI-MEMS technology. *IEEE Sens. J.*, **5**(6):1214-1223. [doi:10.1109/JSEN.2005.857876]

Wang, J., Shang, Y., Tu, S., Liu, L., Chen, D., 2011. Micro-Machined Resonant Accelerometer with High Sensitivity. 6th IEEE Int. Conf. on Nano/Micro Engineered and Molecular Systems, p.527-530. [doi:10.1109/NEMS.2011.6017409]

Wu, X.P., Ko, W.H., 1989. Compensating corner undercutting in anisotropic etching of (100) silicon. *Sens. Actuat.*, **18**(2):207-215. [doi:10.1016/0250-6874(89)87019-2]

Zhang, Q., Liu, L., Li, Z., 1996. A new approach to convex corner compensation for anisotropic etching of (100) Si in KOH. *Sens. Actuat. A*, **56**(3):251-254. [doi:10.1016/S0924-4247(96)01312-X]